










ORIGINAL ARTICLE

Fatigue response of additively manufactured Maraging Stainless Steel CX and effects of heat treatment and surface finishing

Snežana Ćirić-Kostić¹  | Dario Croccolo²  | Massimiliano De Agostinis²  |
Stefano Fini²  | Giorgio Olmi²  | Luca Paiardini²  | Francesco Robusto²  |
Zlatan Šoškić¹  | Nebojša Bogojević¹ 

¹Faculty of Mechanical and Civil Engineering in Kraljevo, University of Kragujevac, Kraljevo, Serbia

²Department of Industrial Engineering (DIN), University of Bologna, Bologna, Italy

Correspondence

Giorgio Olmi, Department of Industrial Engineering (DIN), University of Bologna, Bologna, Italy.

Email: giorgio.olmi@unibo.it

Funding information

Ministry of Education, Science and Technology; European Commission; Horizon 2020; European Union

Abstract

This paper deals with the novel topic of the fatigue response of additively manufactured Maraging Stainless Steel CX. A two-by-two factorial plan was arranged, to experimentally assess the effects of heat treatment and machining on the fatigue strength in both finite and infinite life domains. The two factors were regarded as on–off, taking the untreated unmachined condition as a reference for comparisons. Cylindrical specimens with vertical build orientation were involved in the fatigue campaign under four-point rotating bending. The results indicate that the fatigue strength may be remarkably incremented (up to five times) with respect to the as received conditions, especially thanks to surface smoothing and taking advantage of a very low porosity level. Heat treatment strengthening mechanisms were also interpreted in the light of optical and electron microscope observations. Fatigue enhancement arises from precipitate size increment throughout the conducted heat treatment, although the fracture mode turns to be more brittle.

KEYWORDS

fatigue, heat treatment, Maraging Stainless Steel CX, powder bed fusion, surface finishing

1 | INTRODUCTION

Metal additive manufacturing technologies are nowadays widely used in many industrial fields. Parts are made by merging material powder by a laser source or an electron beam. The components can be built directly from a 3D model, thus reducing the time from conception to market. The model is sliced in layers, a dispenser deposits a layer of powder on a build platform and a laser or an electron beam selectively fuse the corresponding cross-

section of the considered layer. Afterwards, the build plate moves by an amount corresponding to the height of the molten layer. Then, a further powder layer is spread again over the build platform and the aforementioned steps are repeated again until part completion. Thus, the consolidated metallic material within close scans and overlapped melted pools gradually generates the fabricated component.^{1,2}

These additive manufacturing methodologies are often regarded as “powder bed fusion (PBF)”.³ The

This is an open access article under the terms of the Creative Commons Attribution License, which permits use, distribution and reproduction in any medium, provided the original work is properly cited.

© 2021 The Authors. *Fatigue & Fracture of Engineering Materials & Structures* published by John Wiley & Sons Ltd.

possibility of melting material only where necessary makes it possible to build complexly shaped components in a monolithic form,⁴ avoiding material powder waste. Moreover, this procedure makes it possible to achieve a high stiffness to weight ratio. The main application fields involve biomedical, automotive, aerospace, and injection molding industries. The two most widely used powder bed processes are called *DMLS* (direct metal laser sintering) and *SLM* (selective laser sintering),^{5–7} which can nowadays be regarded as synonyms.⁸ Therefore, in the following, they will be regarded as *PBF* processes.

Static and dynamic mechanical properties of components made in *AM* are often different from those of parts made of wrought material. A lot of studies are available in the literature^{9–11} regarding static properties; in addition further data are often yielded by powder supplier datasheets. On the other hand, an extensive use of additively processed parts requires a good awareness of their fatigue properties. The lack of knowledge regarding these items is often regarded as a drawback, mainly affecting new powder materials specifically developed for *AM*. A 0.5 ratio between fatigue limit and ultimate tensile strength (UTS) is commonly accepted for metallic wrought materials,¹² but this generally does not apply to additively processed parts.^{13,14} In addition, products built by additive processes are often affected by defects, such as internal voids and porosities, oxides, as well as poor surface finishing. Tensile residual stresses are also generally present, as an effect of heating and cooling stages with remelting¹⁵ upon the stacking process. These features detrimentally affect the fatigue response.^{16,17} Heat and surface treatments are expected to improve the performance by changing the microstructure^{18,19} or by dropping down the level of tensile residual stresses. Machining may improve surface finishing, also removing the surface layer, in particular surface contours, where defects are generally more concentrated. The effect of roughness or, more generally, of surface irregularity has been the topic of a few papers in the literature that have highlighted the detrimental effect of poor surface finishing. In previous studies^{20,21} it has been shown that roughness level is inversely proportional to fatigue strength, meaning that the higher the roughness, the worse the fatigue response. A possible reason for this outcome is highlighted in several papers, such as^{22,23}: High roughness causes an increase of initiation sites for surface cracks. The higher the surface profile irregularity, the higher the number of onset points. Consequently, many close cracks may start and then propagate fast, due to the high driving force arising from multiple cracking. A further point, when considering additively manufactured as built parts, is that build orientation may also affect the level of induced roughness. The detrimental effect of

roughness involves the fatigue response of a large set of materials, ranging from metals, Al and Ti alloys to Inconel. In Vayssette et al.²⁴ the detrimental effect of roughness was also the subject of a numerical model that was implemented to interpret the fatigue strength of Ti-6Al-4V samples.

A further factor that is likely to affect the performance of additively processed parts is shot-peening. It is a widely used surface treatment that has a positive effect against fatigue and can be applied to several materials, including stainless steel and metal alloys.²⁵ Its main capabilities include the reduction of porosity and the generation of a beneficial compressive residual stress state at the surface and just beneath it. Previous studies on additively manufactured Ti6Al4V have highlighted fatigue strength enhancement²⁶ in preheat treated samples that have been fatigued under four-point rotary bending. The fatigue response improvement arises from negative residual stresses that have the capability of retarding surface crack propagation. This mechanism relies in cracks needing greater cyclic stress levels to grow up to final breakage, even though surface is made more irregular than in the ground state. In addition, the scatter affecting fatigue strength and *S-N* curves is also reduced.²⁷ However, sometimes, surface damage due to the treatment may trigger the initiation of a few surface cracks. The beneficial impact of shot-peening is also highlighted in O'Brien JM et al.,²⁸ where a numerical analysis, involving an additively processed stainless steel, has been run. Its results indicate that heat treatment and shot-peening have the capability of relaxing the stacking process-induced tensile residual stresses and, in addition, of generating a significantly compressed layer at the surface. Some authors have also observed an effect of grain refinement.^{29,30} This point is also highlighted in Almangour and Yang,³¹ where additively fabricated 17-4 stainless steel was initially shot-peened and subsequently heat treated. It was observed that the peening/heat treatment combination has the capability of inducing a finer microstructure, precipitate growth, and larger martensitic volumes that are likely to positively affect the material mechanical response.

Process parameters, such as build orientation, are also important, as well highlighted in Todai.³² Both the overall number of layers being needed to manufacture a part and the time for scanning a layer are highly dependent on part orientation on the build platform. For example, when fabricating a cylindrical sample lying on the plate, a reduced number of layers is needed, but laser scans of each section are remarkably long and take a longer time with respect to a vertically oriented specimen. Some of the aforementioned factors have been investigated by the authors in previous studies involving different

materials,^{13,14,33,34} including Maraging and Stainless steels. Maraging steels have wide applications in many fields, with particular regard to automotive, aeronautics, and tool machine industry. Previous studies, such as that in Kempen et al.,³⁵ investigated the influence of some processing and postprocessing parameters and treatments on the static properties of additively manufactured Maraging Steel grade 300. The retrieved responses were also compared with the performance of wrought material. Other studies involving Maraging steels have been focused on the effects of internal defects or voids³⁶ or of microstructural features³⁷ on fatigue.

Several researches in the literature deal with stainless steel mechanical static and fatigue properties, as an effect of additive process and postprocess parameters.^{21,38,39} Stainless steel CX can be regarded as a recently introduced Maraging Stainless Steel featuring a low carbon content and a high amount of chromium. These characteristics lead to interesting properties such as remarkable corrosion resistance, high hardness, and *UTS* as well as yield point (*YP*). Moreover, this alloy may be classified within precipitation hardening stainless steels that take advantage of the precipitation of the β -NiAl intermetallic phase.⁴⁰ EOS GmbH has recently introduced the feedstock powder for this material (named stainless steel CX or Corrax[®]) that can be processed by *PBF* machines. Consequently, this alloy is a valid candidate for injection molding tools even in harsh environments^{41,42} and also for shipbuilding, constructions in oil and gas field, offshore technologies, and nuclear power plants.⁴³

The few papers dealing with Stainless steel CX in the scientific literature are focused on microstructural properties, hardness, and microhardness features and only static response. The study in Asgari and Mohammadi⁴² deals with microstructural microscope observations to identify scan tracks and melted pools, whose dimensions were compared with printing parameters. X-ray diffraction was also run, thus highlighting weak peaks of austenite and much sharper ones of martensite. Static strength hardness and porosity levels were investigated as well, emphasizing a nearly full dense structure. Potential anisotropy arising from different build orientation was studied in Sanjari et al.⁴⁴ Microstructural features and micromechanical properties (hardness, response to nanoindentation) were investigated, highlighting differences arising from different printing strategies. Other studies^{45,46} are focused on the effect of heat treatment on static properties, in particular microhardness and, consequently, strength. The response in as built conditions was compared with those following austenitization only, aging only, or austenitization with subsequent aging, which is the treatment being recommended by the powder supplier (EOS,⁴¹). The paper⁴⁶ also deals with heat

treatment effects on toughness, whereas a further study⁴⁷ is focused on CX corrosion resistance, which is remarkably enhanced for CX with respect to same class materials.

As exposed above, additive manufacturing has great potentials for rapid manufacturing of highly complicated parts as single components. However, previous studies, involving other materials, highlighted that the stacking process may lead to a lower fatigue strength with respect to corresponding wrought materials. In fact, as above, for conventional wrought materials, the fatigue limit for infinite life may be coarsely estimated as the half of their *UTS*,¹² but this ratio is significantly dropped down, when considering an additively processed material. For this reason, a lot of research is needed in this field, in order to investigate the relationship between the additive process and the achievable fatigue response, accounting, in case, for postfabrication stages.

However, it is clear that the topic of fatigue involving CX is still unexplored despite its importance in many industrial applications. In addition, postmanufacture treatments, in particular heat treatments, as highlighted in^{48,49} and surface machining, may be used to enhance its fatigue strength. No study is available regarding the effect of the aforementioned postprocessing and on their interaction on fatigue in the finite or infinite life domains. A further important point is that this Maraging Stainless Steel is likely to have a different behavior with respect to other Maraging or stainless steels. In fact, unlike conventional Maraging steels, featuring 18 wt% Ni and being strengthened by Ni₃Ti precipitates, CX composition accounts for a much lower content of Ni, just 8 wt%. Moreover, it is strengthened by the precipitation of its β -NiAl intermetallic with an ordered CsCl superlattice.^{40,44,47} On the other hand, Stainless Steel CX, when compared with other Stainless Steels, has a much lower C content and a much higher Cr concentration, up to 11%, which has been exploited to improve its anti-corrosion properties, as remarked in previous studies.^{42,47}

This paper tackles the topic of additively manufactured CX under fatigue, following different treatments by an experimental approach with subsequent statistical assessment of the data. Fractography, micrography, hardness and porosity estimations, and scanning electron microscope analyses have been utilized to interpret the data and to investigate the strengthening mechanisms. Based on the aforementioned remarks, evident issues of novelty arise from the point that this study is the very first that deals with the fatigue response of this material being significantly different from the other Maraging Stainless Steels.

2 | MATERIALS AND METHODS

The material involved in the present research is the aforementioned Maraging Stainless Steel CX, having a mainly martensitic structure, supplied by EOS GmbH – Electro Optical Systems, Krailling/Munich, Germany. Its composition is provided in Table 1.

All the specimens were manufactured using EOSINT M290 machine equipped with Ytterbium fiber laser with 400-W power, with working space 250 mm wide and 250 mm long. All the samples were produced during a single production process (one batch) with vertical orientation of longitudinal axis of the samples during production process. The production process used the EOS standard direct part set, recommended as default for industrial applications, with layer thickness of 30 μm and building volume rate of 3.2 mm³/s. Fresh powder was used for sample production, meaning that totally new (not recycled) powder was used upon fabrication.

The developed experimental plan involved two factors, both regarded over two levels. The first factor was the heat treatment: the response without and with heat treatment was assessed. The second factor concerned machining: The response of unmachined samples, to be regarded as the zero level, was compared with that of ground specimens. Postmanufacture heat and surface treatments were run, according to the protocol and sequence being detailed below.

The experimental design is summarized in Table 2: Four sets were built: “NN” (not heat treated and not machined), “HN” (heat treated and not machined), “NM” (not heat treated and machined), and “HM” (heat treated and machined). Fifteen specimens were built per combination, corresponding to a total of 60 samples. These were shaped according to Standard ISO 1143, with uniform cross-section at gage. After the stacking process, the samples of the “NN”-type underwent shot-peening according to the procedure and the parameters provided below. According to the literature^{50–52} and to EOS recommendations, this treatment is usually carried out to close the surface porosities and to generate a beneficial compressive residual stress state aiming at balancing the stacking process-induced tensile residual stresses. Set HN samples were treated by shot-peening, as mentioned above, and then underwent heat treatment according to the following procedure. This was split into two stages: Solution annealing and aging,^{41,48,49} whose details are

provided in the points below. The two-step heat treatment is designed to get homogeneously distributed fine precipitations (which are extremely hard) in the relatively soft and ductile metallic matrix. According to the powder supplier, this process makes it possible to achieve excellent properties of hardness, strength as well as ductility for the treated part.

- Solution annealing
- Heating up to 900°C with heating rate around 5.5–6°C/min.
- Parts kept at the controlled temperature of 900°C for 45 min.
- Rapid cooling in compressed air stream from 900°C to 150°C with 150°C/min cooling rate.
- A further cooling from 150°C to room temperature with cooling rate around 10°C/min.

Aging phase

- Heating from room temperature to 530°C with heating rate around 5.5–6°C/min.
- Parts kept at the controlled temperature of 530°C for 3 h.
- Cooling in a furnace to the room temperature.

It must be remarked that it is consistent with that recommended by EOS in a previous study.⁴¹ However, very few details are available in the scientific literature and in supplier datasheets regarding the practical procedure to conduct this treatment and especially to comply with the strict specifications related to cooling or heating rates. From this point of view, the conducted procedure was highly demanding, as it required a controlled argon flow (around 1.5 L/min) to assist heating as well as rapid cooling. According to a previous study,⁴¹ the *UTS* is enhanced from 1080 to 1760 MPa, following heat treatment. Similarly, its *YP* is also incremented from 840 to 1670 MPa.

Samples of the “NM” type were initially ground with 0.5-mm allowance. Afterwards, they underwent shot-peening according to the same specifications. In previous studies dealing with Maraging Steel, it was found that beneficial effects are given on the fatigue response by peening treatment when it is performed after machining.³⁴ As highlighted in this Reference, powder suppliers usually recommend running shot-peening before machining. However, proceeding this

Cr (%)	Ni (%)	Mo (%)	Al (%)	Mn (%)	Si (%)	C (%)	Fe (%)
11–13	8.4–10	1.1–1.7	1.2–2	≤0.4	≤0.4	≤0.05	Bal.

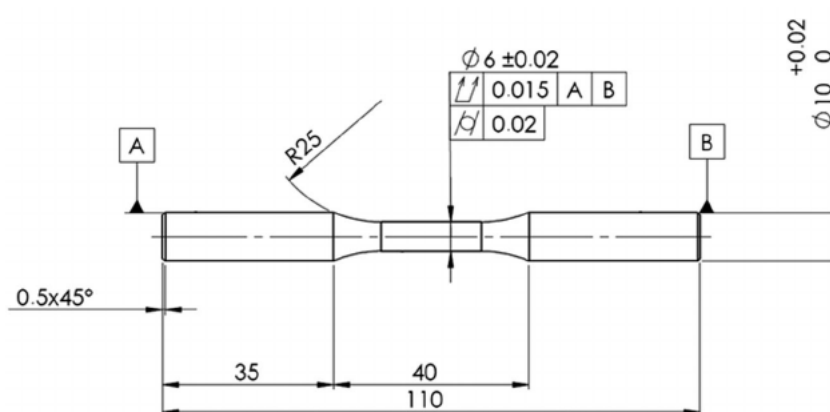
TABLE 1 Chemical composition of Maraging Stainless Steel CX (wt%)

TABLE 2 Experimental plan

		Factor 2: surface condition	
		Shot-peened	Machined and shot-peened
Factor 1: heat treatment	Not heat treated	Type NN	Type NM
	Heat treated	Type HN	Type HM

Abbreviations: HM, heat treated and machined; HN, heat treated and not machined; NM, not heat treated and machined; NN, not heat treated and not machined.

FIGURE 1 Specimen with 6-mm diameter at gage, 10 mm at the heads complying with ISO 1143 standard (all dimensions in mm)



way, the treated layer is completely removed, thus making the peening treatment barely ineffective. Conversely, running shot-peening after grinding makes it possible to take advantage of the peening-induced compressive residual stress state. Since this beneficial effect is not strictly related to material properties, it is reasonable to presume that it may also apply to the CX Maraging Stainless Steel. For this reason, for machined sets, shot-peening was always conducted after machining.

Finally, regarding samples from the HM Sets, after the end of the *PBF* process, they initially underwent heat treatment as exposed above. Afterwards, they were ground with 0.5-mm allowance and finally shot-peened according to same parameters of the other sets, which are going to be provided in the following paragraph.

As a final resume, regardless of the sample set they were belonging to, all the specimens had their surfaces treated by shot-peening. For the sake of clarity, it was run just after *PBF* for Sets NN and HN and after machining for Sets NM and HM. The involved shots were made of stainless steel and had 0.43-mm average diameter (corresponding to S170) and 47 HRC average hardness. Airstream pressure was 8 bar, which led to 0.55 m³/min air consumption (in normalized air conditions). Airstream orientation was kept perpendicular to the sample surface, at 50-mm distance, throughout the entire process.

3 | EXPERIMENTAL

The specimens were made with smooth cylindrical shape in agreement with ISO 1143. The gage diameter was set at 6 mm. This value is the minimum recommended in the standard and could be regarded as a good trade-off between standard specification accomplishment and cost saving. The heads were produced with 10-mm diameter. A specimen sketch is provided in Figure 1.

Prior to experimental testing, all the samples were checked for dimensions and roughness with a suitable number of replications for statistical evidence reasons. For this purpose, an electronic micrometer (resolution of 0.001 mm) and a portable surface roughness tester with the resolution of 0.001 μ m (RT25, by SM Metrology System, Torino, Italy) were used. Six diameter measurements were run at the gage and four at each head. Roughness measurements were carried out both at gage and at both heads with eight replications. Ra is averagely 6.3 μ m for unmachined shot-peened samples (Sets NN and HN). Machining has clearly the capability of remarkably dropping down roughness values. Subsequent shot-peening leads to the final observed values around 1 μ m (average value: 1.5 μ m) being consistent with those for peened surfaces.³⁴

The tests were performed by a four-point rotating bending machine (RB 35, by Italsigma, Forlì, Italy), controlled by a computer, which makes it possible to have a

constant bending moment at the gage and a stress ratio $R = -1$. This symmetrical alternating load has been utilized in many researches aimed at the investigation of the fatigue response of additively processed parts.⁵³ The load frequency was set at 80 Hz, complying with a previous study.⁵⁴ The samples were fatigued until failure or up to 10^7 cycles, to be regarded as run-out. The run-out value was chosen in agreement with previous campaigns involving Stainless Steel PH1 as well as Maraging steel.^{33,34} Before each test, sample misalignment at gage was checked by a centesimal comparator.

The tests were devoted to the determination of the $S-N$ curves in the finite life domain and of the fatigue strengths at 10 million cycles (FL). The $S-N$ curves were determined complying with Standard ISO 12107, determining confidence bands corresponding to 10% and 90% probabilities of failure and 90% confidence level. According to standard recommendations, both the linear and the quadratic model were implemented and the general linear test was applied to assess whether the improvement yielded by the quadratic model was significant. However, it always proved to be negligible; therefore, the linear interpolation model was applied instead. FL s were worked out by abbreviated staircase (averagely, seven nominal specimens) based on the Dixon method,⁵⁵ which is applied in several studies such as.⁵⁶ Confidence bands at the 90% confidence level were applied as well, based on fatigue limit standard deviation and on the size of the sequence at staircase. Density analyses were performed by the immersion method to estimate the porosity level of the specimens. These tests were aimed at comparing the relative density in the treated and in the untreated states to literature reference data. This analysis was also aimed at assessing the comparability of the retrieved microstructural properties to those observed in other studies dealing with static properties of CX. The measurements were carried by an electronic balance based on the Archimedes principle. The weight of the specimens was measured twice: the first measurement was made in air. The second one was performed with the specimens immersed in distilled water. The difference between the two measurements is equal to Archimedes' thrust (or hydrostatic lift). It made it possible to estimate the overall volume of the sample and consequently its density to be compared with the theoretical one for the material. Their ratio yielded the relative density, whose deviation from 100% is related to the porosity level.

To furtherly assess the porosity level, an image analysis was also carried out. Three specimens per types were cut by a saw: one cross-section and two longitudinal sections were obtained from each sample. The sections were carefully polished by sandpaper and a water and alumina

solution. Afterwards, some surface pictures were taken by a Stemi 305 stereo-microscope (by ZEISS, Oberkochen, Germany). The polished surfaces, under the stereoscope light, appear black except for porosity areas, which are conversely very bright. By an image processing software, the proportion between dark pixels and white ones was evaluated, thus providing an estimation of the porosity level.

Rockwell hardness (HRC) measurements were carried out, running 3 measurements per sample and 45 measurements per sample type. Hardness tests were carried out both in the not heat treated and in the treated conditions in order to compare the retrieved results to literature data. This analysis was important to ensure the conformity of the material and of the performed heat treatment and the alignment of mechanical properties to those observed in other studies addressing CX static properties. Machined samples only were involved in this analysis in order to avoid hardness measurements being altered by surface asperities in the unmachined ones. In particular, 120° equally spaced spots at sample heads were involved in hardness assessments. The results were worked out based on the recommendations in⁵⁷ in order to consider the actual convex surface curvature, thus properly correcting the experimental yields.

Fracture surfaces were then analyzed, to individuate crack nucleation sites and to highlight any internal defects, oxides, or porosities. A Stemi 305 stereo-microscope (by ZEISS, Oberkochen, Germany) and an Optiphot-100 optical microscope (by Nikon, Melville, NY, United States) were utilized for this purpose.

The microstructure induced by the stacking process, with and without heat treatment, was initially investigated by micrographies. For this purpose, three samples per group were cut along the cross-section and along their longitudinal section, which made it possible to investigate the microstructure on the deposition plane and along the vertical stacking direction and to address the effect of heat treatment. Vilella's reagent with surface preheating was utilized as chemical etchant, and the aforementioned optical microscope was used.

At the last stage, observations by a scanning electron microscope (SEM) were run. These analyses were again aimed at assessing the microstructure in the as-built condition and following heat treatment, thus assessing heat treatment strengthening effect. Furthermore, fracture surfaces in the same conditions were observed, to explore fatigue propagation and different final fracture mechanisms. This microscope (Mira3 Model, by TESCAN, Brno, Czech Republic) is equipped with a hot-cathode field emission gun (tungsten filament emitter) and with an energy-dispersive X-ray spectroscopy (EDS).

4 | RESULTS

All the fatigue results were processed by the linear model according to Equation 1, which can be turned into Equation 2. The calculated coefficients b_0 and b_1 are collected in Table 3. Figure 2 shows all the fatigue $S-N$ curves in the finite life domain along with the related experimental points.

$$\text{Log}(N) = b_0 + b_1 \cdot \text{Log}(S) \tag{1}$$

$$S = 10^{\frac{b_0}{b_1}} \cdot N^{-\frac{1}{b_1}} \tag{2}$$

Density analysis was also performed by the immersion method, as detailed in the methodological Section. The values for each set are shown in Table 4, in terms of

TABLE 3 Coefficients of the determined $S-N$ curves, according to the linear model of ISO 12107

Set #	b_0	b_1	$10^{b_0/b_1}$	$-1/b_1$
NN	9.441	1.768	218,742	-0.566
HN	18.955	5.354	3,470	-0.187
NM	52.247	17.114	1,129	-0.058
HM	21.559	5.390	9,996	-0.186

Abbreviations: HM, heat treated and machined; HN, heat treated and not machined; NM, not heat treated and machined; NN, not heat treated and not machined.

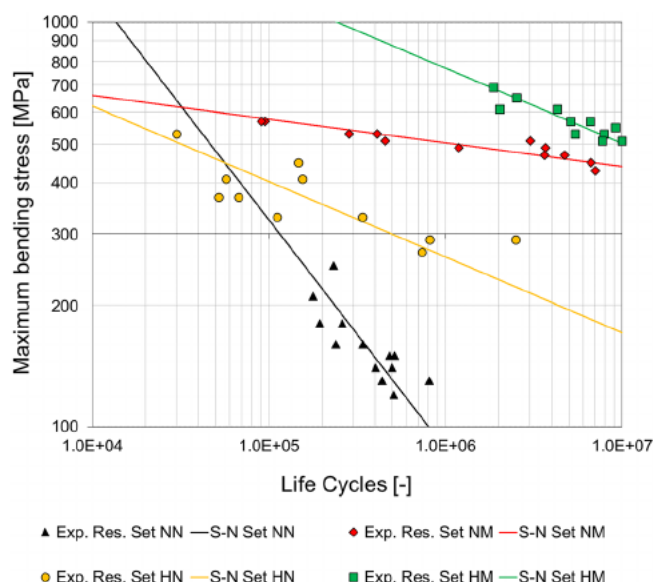


FIGURE 2 $S-N$ curves in the finite life domain for all the samples [Colour figure can be viewed at wileyonlinelibrary.com]

average density and as a percentage with respect to the declared data by EOS⁴¹ that is equal to 7,700 kg/m³.

Considering that relative density estimates are highly affected by the declared value by the supplier, a further analysis was carried out. As reported above, three specimens per type were cut along the longitudinal and transverse directions. The surfaces were then polished and observed by stereoscopic measurement. In these conditions, without any chemical etching, a large part of the area generally appears black. The presence of porosities is highlighted by a different light reflection that makes them appear bright. The images were then processed, turning them into grayscale and reversing the colors.

A processed image with inverted colors is displayed in Figure 3A with reference to a longitudinal section (i.e., along the sample main axis of inertia, along the build direction) of a machine sample. Another image is shown in Figure 3B with regard to an unmachined sample. In this case, a cross-section (build surface) is displayed. Related details, with corresponding scales, are provided in Figure 3C,D, respectively. In these images, voids and porosities are highlighted by dark shadows in a white landscape: The amount of black may be easily determined by graphic processing with the aid of several freeware software. Therefore, the ratio between the black and the white pixels can be regarded as a reliable indicator of the porosity level in the investigated area. This outcome, if confirmed by similar analysis on the same component, may be extended to the entire part.⁵⁸ The retrieved data indicate the porosity level is consistent for all the sample sets: It is in particular 0.1% for NN, HN, and NM Sets, and a bit high, up to 0.3% for the HM Set.

Hardness measurements (HRC) are 31.0 ± 1.5 , when considering not heat treated material (set NM) and 47.0 ± 0.9 for heat treated material (set HM). Confidence intervals take the worst scenario of twice the standard deviations into account.

The study was completed by fractographic and micrographic analyses by stereoscopic and optical

TABLE 4 Density measurements

	Measured density (kg/m ³)	Relative density (declared density by EOS ⁴¹ : 7,700 kg/m ³)
Set NN	7,651	99.4%
Set HN	7,631	99.1%
Set NM	7,674	99.7%
Set HM	7,666	99.6%

Abbreviations: HM, heat treated and machined; HN, heat treated and not machined; NM, not heat treated and machined; NN, not heat treated and not machined.

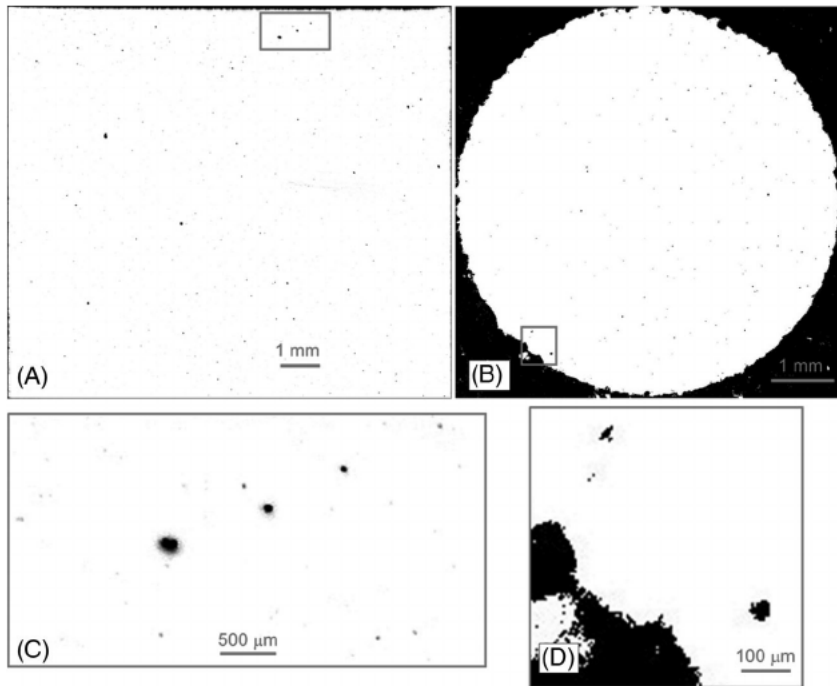


FIGURE 3 (A) Graphically processed polished longitudinal section of a machined sample. (B) Graphically processed polished cross-section of an unmachined sample. (C) A detail of (A). (D) A detail of (B) with visible subsurface porosities [Colour figure can be viewed at wileyonlinelibrary.com]

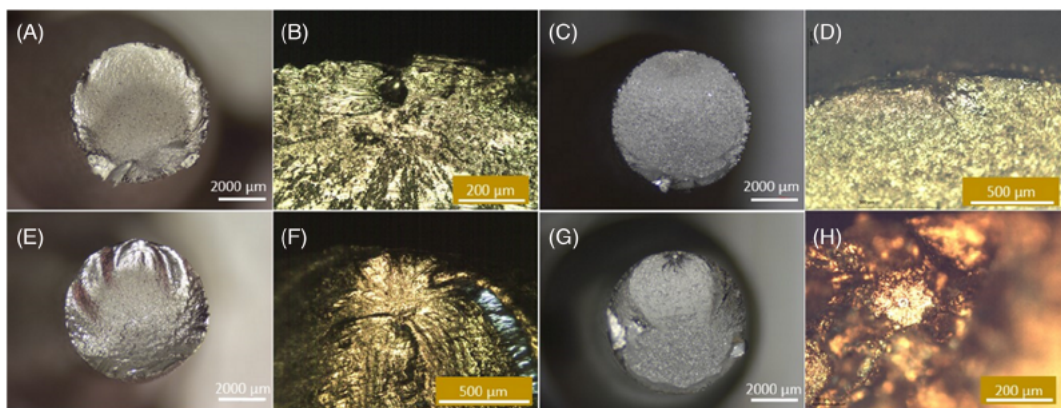


FIGURE 4 Fracture surfaces observed by stereoscope (A, C, E, F) and by optical microscope (B, D, F, H). Sample numbers: NN08 (A, B); HN05 (C, D); NM05 (E, F); HM13 (G, H) [Colour figure can be viewed at wileyonlinelibrary.com]

microscopes. Some fracture surfaces are shown in Figure 4. The outcomes of micrographies captured by optical microscope are shown in Figures 5 and 6. The first one refers to not heat treated specimens (NN and NM Sets), whereas the latter deals with heat treated ones (from HM Set).

5 | DISCUSSION

5.1 | Statistical assessment

The plots in Figure 2 suggest that both machining and the heat treatment have a positive effect on the fatigue

performance. An ANOVA-based extended statistical method for the comparison of trends, which was first introduced in a previous study⁵⁹ and then successfully adopted in other studies,^{13,14,34} was applied here to properly compare the $S-N$ curves. In particular, the tool of two-factor design has been utilized in order to assess whether the visible differences among the curves are significant, if compared with the scattering of the experimental campaign. The curve trends were compared, averaging their differences over the lifespan ranging from 10^4 to 10^7 cycles, which corresponds to the observed lifespan. The analysis starts with the computation of the gran mean curve \bar{S} , to be computed as reported in Equation 3.

FIGURE 5 Micrography surfaces.
(A) Sample NM09, longitudinal section.
(B) Sample NN01, cross-section (melt pool boundaries highlighted by red dashed lines)
[Colour figure can be viewed at
wileyonlinelibrary.com]

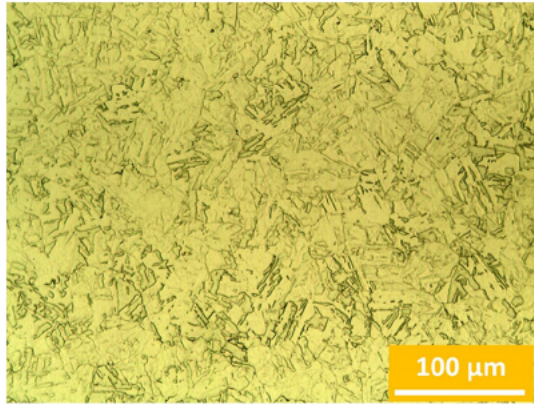
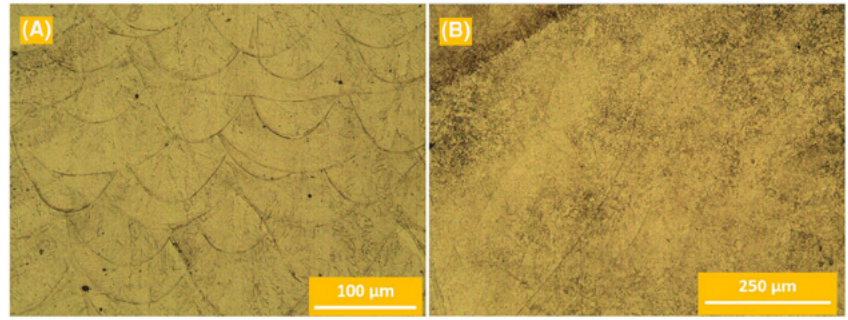


FIGURE 6 Micrography involving a heat treated sample (from Set HM) [Colour figure can be viewed at wileyonlinelibrary.com]

$$\bar{S} = \frac{S_{NN} + S_{HN} + S_{NM} + S_{HM}}{4} \quad (3)$$

S_{xx} indicates the 10-base logarithm of the stress corresponding to a generic fatigue life, whereas the subscript corresponds to the previously mentioned sample sets. The second step of the analysis consists in the computation of the row means (R_1 and R_2) and of the column means (C_1 and C_2), where

$$R_1 = \frac{S_{NN} + S_{NM}}{2} \quad (4)$$

$$R_2 = \frac{S_{HN} + S_{HM}}{2} \quad (5)$$

$$C_1 = \frac{S_{NN} + S_{HN}}{2} \quad (6)$$

$$C_2 = \frac{S_{NM} + S_{HM}}{2} \quad (7)$$

Then, the $SSBR$ and the $SSBC$ terms have been computed. The $SSBR$ term (sum of square between rows) takes the effect of the “Row” factor into account. Consequently, based on the experimental design in Table 2, this

term deals with the effect of heat treatment comparing the fatigue trends with and without this postprocessing (Equation 8). The $SSBC$ term (sum of square between columns) is related to the effect of the “column” factor, that is, machining. The fatigue response with and without grinding is consequently compared (Equation 9). Like in conventional $ANOVA$, sums of the squares of the differences between row and column means and the grand mean are computed

$$SSBR = (R_1 - \bar{S})^2 + (R_2 - \bar{S})^2 \quad (8)$$

$$SSBC = (C_1 - \bar{S})^2 + (C_2 - \bar{S})^2 \quad (9)$$

Setting $S_{1,1} = S_{NN}$, $S_{1,2} = S_{NM}$, $S_{2,1} = S_{HN}$, and $S_{2,2} = S_{HM}$, based on the position of these treatment combinations in the matrix in Table 2, it is finally possible to calculate the term $R_i C_j$ as shown in Equation 10. This term makes it possible to compute SSI term, being the acronym of sum of squares interaction and taking the interaction between the two mentioned factors into account.

$$R_i C_j = S_{ij} - R_i - C_j + \bar{S} \quad (10)$$

and then the SSI term (Equation 11).

$$SSI = \sum_{i=1}^2 \sum_{j=1}^2 R_i C_j^2 \quad (11)$$

The aforementioned terms were computed over the entire lifespan with a sufficiently refined step. Afterwards, they were turned into scalars, taking the respective integral means over the entire life range in order to have global indicators being reliable of the average impacts of factors and interaction over the investigated life domain.

The last term we need to compute the $ANOVA$ analysis is the error-related term SSE . It can be regarded as the sum of the squares of the residuals between the

experimental data distributions and the retrieved $S-N$ curves. This term may be estimated, based on Equation 12, where S_{exp} represents the logarithm of the stress level corresponding to an observed life and S_{calc} indicates the same stress level in the logarithm scale, based on the interpolated $S-N$ curve for the same life extent. In this formula, the subscripts i and j retain the same meanings as above, indicating the rows and the column of the experimental design in Table 2, whereas k identifies the k -th experimental point and n_{ij} is the number of available points of the dataset.

$$SSE = \sum_{i=1}^2 \sum_{j=1}^2 \sum_{k=1}^{n_{ij}} (S_{exp_{i,j,k}} - S_{calc_{i,j,k}})^2 \quad (12)$$

A final step was needed to make the determined terms comparable with one another and to process them in a conventional two-factor ANOVA: The aforementioned terms were scaled, rationalizing them by the related degrees of freedom. The outcome of the statistical assessment is reported in Table 5 and can be commented with reference to the plots in Figure 2. The conclusion was that both heat treatment and machining significantly affect the fatigue life. Moreover, the two factors have a strong interaction. Glancing at the plots in Figure 2, it is possible to highlight the heat treatment effect. The curves of the heat treated specimens HN and HM are generally higher than those for not heat treated conditions, that is, NN and NM. This outcome highlights that the performed heat treatment remarkably enhances the fatigue strength regardless of surface conditions. At the same way, curves for sets with and without machining can be compared: NM and HM series generally exhibit higher strength than the unmachined Sets NN and HN. The interaction effect may also be discussed, based on curves trends. This point may be addressed, comparing the slopes of the curves, being related to the coefficient b_1 (Table 3) of curve equations in the logarithmic scale. Interaction generally arises from a different effect of one factor, depending on the current level of the other

one. In the curves of the HN and HM series, the coefficient b_1 assumes approximately the same value and, in fact, their slopes keep approximately the same. This means that for heat treated series, the improvement yielded by surface grinding is the same both for low and for high life cycles regimes. On the other hand, the $S-N$ curves for the NN and NM Sets have considerably different slopes and their b_1 coefficients are also highly different. This outcome indicates that, when heat treatment is not performed, machining leads to a fatigue enhancement, which is remarkably greater at higher life spans. Therefore, the effect of machining is different in untreated and treated parts and is significantly incremented on not treated parts. A similar remark applies to heat treatment effect that keeps different for unmachined and machined parts.

5.2 | Fatigue strengths at 10 million cycles and most noticeable parameter combinations

The fatigue curves along with their confidence bands are singularly plotted in Figure 7. FL nominal values are displayed in the bar graph in Figure 8, where the corresponding confidence intervals at the 90% confidence level are also appended to the bars. The bar graph highlights and confirms the beneficial effects of both heat treatment and machining. Taking the samples type NN (not treated and not machined) as a reference, heat treatment without machining leads to more than doubled FL . On the other hand, machining without heat treatment has the capability of remarkably incrementing the FL by a factor three. The combination of heat treatment and machining with subsequent shot-peening leads to a further improvement: The FL for Set HM appears to be more than four times increased with respect to that for type NN. This is indeed the best combination of the four. The reasons for this result can be justified based on several argumentations.

TABLE 5 Analysis of variance results

	Sums of squares	Degrees of freedom	Sums of squares after scaling	Fisher's ratio	p -value
SSBR: effect of heat treatment	0.0826	1	0.0826	30.85	$2.16 \cdot 10^{-6}$
SSBC: effect of machining	0.2831	1	0.2831	105.65	$1.17 \cdot 10^{-12}$
SSI: interaction	0.0483	1	0.0483	18.03	$1.30 \cdot 10^{-4}$
SSE: error (data scattering)	0.1045	39	0.0027		
Total	0.5185	42			

Abbreviations: SSBC, sum of squares between columns; SSBR, sum of squares between rows; SSE, sum of squares error; SSI, sum of squares interaction.

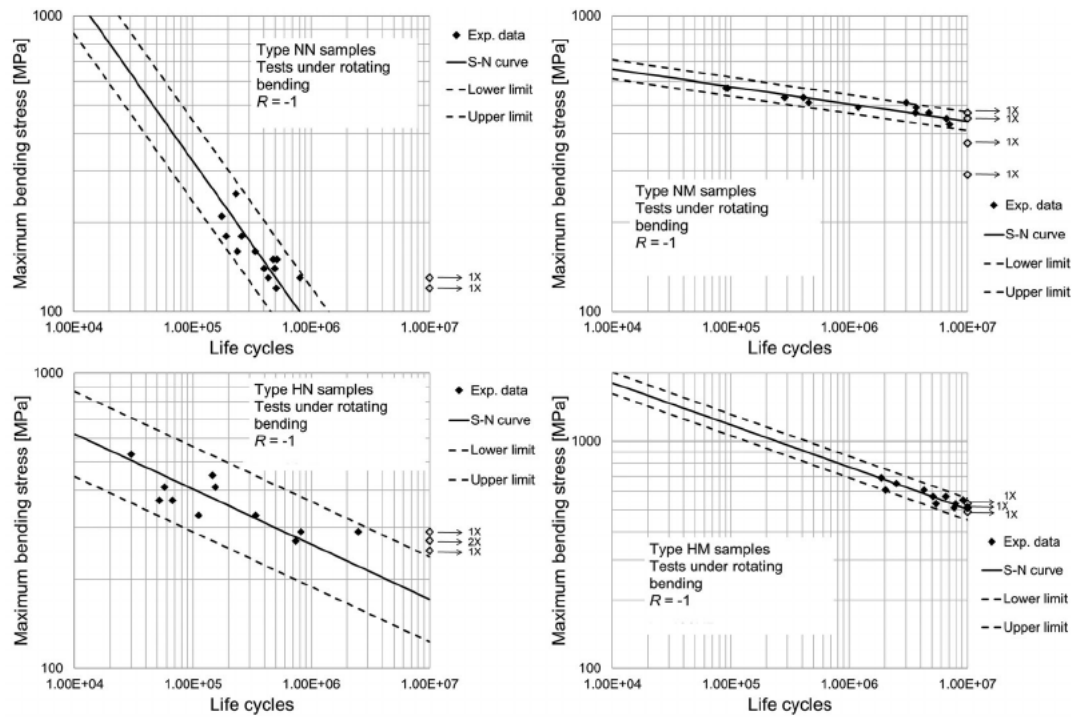


FIGURE 7 S-N curves with upper and lower bounds, according to ISO 12107

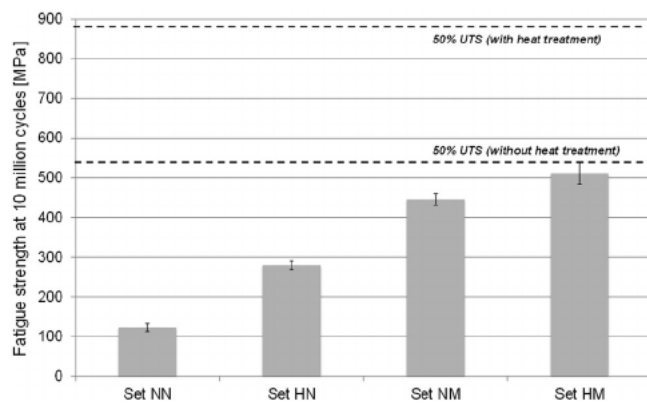


FIGURE 8 Fatigue strengths at 10 million cycles (FL_s)

The machining process indeed drops down surface roughness (R_a), which is reduced from 6–7 μm to 1 μm or even less, thus making the surface smoother and reducing the number of potential crack nucleation sites. As reported in the Section 1, several studies in the literature indicate that a poor finishing worsens the fatigue properties. Furthermore, the removal of the outermost layers erases the external contours that are usually the most affected by detrimental porosities and voids. On the other hand, heat treatment has the capability of relaxing the stacking process-induced tensile residual stresses that detrimentally affect the fatigue response. The main reason for the observed fatigue response must be related to the structure of the investigated Maraging Stainless Steel

with and without heat treatment.^{45,46} When in its as-built state, it consists of columnar or equiaxed cells that feature its martensitic matrix. The structure is completed by fine nanoprecipitates, uniformly spread in the matrix, whose development is triggered by the additive process, in the framework of heating/melting stages, followed by rapid cooling. The precipitate size is furtherly incremented upon the two-stage heat treatment, while new precipitates tend to nucleate. Therefore, the treated material has its hardness and strength incremented with positive outcomes regarding its static and fatigue resistances. Discussion regarding heat treatment strengthening effect is going to be deepened in the following, based on the support of Field Emission Gun Scanning Electron Microscope (SEM-FEG) observations.

An interesting point for design purposes is the estimation of the ratio between the determined fatigue strengths at run-out and the UTS declared by the powder supplier in a previous study⁴¹ with and without heat treatment. To properly tackle this question, two dashed lines have been appended to the bar graph in Figure 8, in order to indicate the levels corresponding to 50% of the UTS in the two conditions above. It is worth mentioning that the ratio versus UTS is sharply incremented by machining, when considering untreated samples: from 0.11 to 0.41. This is also increased for heat treated samples from 0.16 to 0.29. This latter value is indeed lower than the previous one and also keeps much lower than 50% of UTS for treated material.

An important outcome is that the 0.29 *FL* versus *UTS* ratio for treated and machined samples is very close to the corresponding values retrieved for Maraging steel MS1 and for Stainless Steel 15–5 PH1^{13,14,33,34} and, therefore, may be assumed as a reference for design for this class of materials. A further remarkable outcome is that machining parts, even without heat treating them, can be regarded as a highly efficient combination. On the one hand, the ratio over *UTS* is the highest one and very close to 0.5; on the other hand, the corresponding *FL* keeps very close to the highest one retrieved for the heat treated and machined samples (450 MPa against 510 MPa).

5.3 | Density and porosity

The immersion method was used as a first approach to address relative density estimation and to consequently work out the porosity level. As above, running this further analysis was important to compare the retrieved outcomes to other results in the literature for the same (untreated and treated) material in order to make sure of the comparability of static properties and of the correct execution of heat treatments. Not remarkable differences were observed: The retrieved data were all aligned and even greater than the declared value by the powder supplier, that is, 99%. A 0.5%–1% average level of voids is usually commonly accepted and consistent with the specifications of most powder suppliers.^{41,60} Moreover, it is worth mentioning that the obtained results are also well consistent to those in Hadadzadeh et al.,⁴⁵ where a 0.32% porosity level was observed.

The porosity levels were also worked out, following an accurate graphic processing analysis of microscope observation. Consistent data were obtained for all the investigated sections, regardless of part type and of orientation: Average porosity levels range from 0.1% to 0.3%. These outcomes confirm those by the immersion method and are well aligned with those in Asgari and Mohammadi⁴² for the same material, confirming the full density of the stacked parts, regardless of set features. They all confirm that the studied samples are absolutely conformal to common specifications for additively processed parts and to previously investigated CX samples in the literature.

Anyway, considering the captured images (in particular the detail in Figure 3D), it is worth mentioning that, when considering unmachined samples (i.e., NN or HN Sets), a few porosities are located close to the surface, presumably at the interface between the external contour lines and the internal scanned surface.

Hardness values appear to be a bit lower than those included in previous studies^{41,42}: In particular, a difference by four *HRC* has been observed. It is worth mentioning the same discrepancy affects both untreated and treated samples, which indicates that the observed hardness increment, following heat treatment, is completely compliant with previous studies and material specifications.

5.4 | Fractography and micrography

With regard to the fracture surfaces shown in Figure 4, it was found that almost the totality of failure starts from surface defects with multiple nucleation points for not machined specimens (types NN and HN). As highlighted in previous studies,^{21–23} a high surface roughness has the detrimental effect of triggering crack initiation and consequent propagation. Conversely, in most (over 90%) machined samples (NM and HM types), the failure grows up from internal porosities located at a distance from the edge up to 500 μm . This outcome is clearly due to the removal of surface defects and roughness crests, as also confirmed by the much better fatigue response versus unmachined specimens. In addition, part machining with 0.5-mm allowance has also the capability of removing contour lines. Thus, several subsurface defects and voids, which are often present at the interface between laser scans and contour lines (as highlighted above and as it is also visible in the detail in Figure 3D), are also removed.

Micrographies observed by optical microscope are depicted in Figures 5 and 6. The first one refers to not heat treated specimens (NN and NM Sets). The picture in Figure 5A was taken, following a cut along the sample longitudinal section (a plane containing the sample main axis of inertia). Therefore, the microstructure along the vertical stacking direction is here depicted. Conversely, the micrography in Figure 5B refers to a transverse cut along the cross-section, which means the microstructure on the build surface is here investigated. Stacked layers are clearly visible in Figure 5A, whereas laser scans can be observed on the build surface in Figure 5B. The retrieved microstructure is completely different in the heat treated specimens, where the typical structure of additively processed parts is no longer visible and the difference between stacked layers and laser scans also vanishes. A microscope observation is displayed in Figure 6, considering the same chemical etching. This image refers to a longitudinal plane along the build direction, but exactly the same pattern was observed in the perpendicular plane.

5.5 | Heat treatment strengthening effect investigated by SEM-FEG analyses

The microstructure in the as-built and heat treated conditions and the effect of heat treatment were then investigated in the light of SEM-FEG observations. In particular, the analysis involving not heat treated samples has made it possible to get awareness of the

solidification morphology, following the stacking process. The picture in Figure 9A, taken on the build surface, indicates that the solidification process has led to a set of equiaxed and columnar cells, which is in agreement with the outcomes in.^{45,46}

The generation of these morphologies arises from the actual solidification rate and thermal gradient. For instance, a high cooling rate leads to the development of

FIGURE 9 Scanning electron microscope (SEM-FEG) observations in the not heat treated state: (A) equiaxed and columnar cell structures and (B) observed precipitates

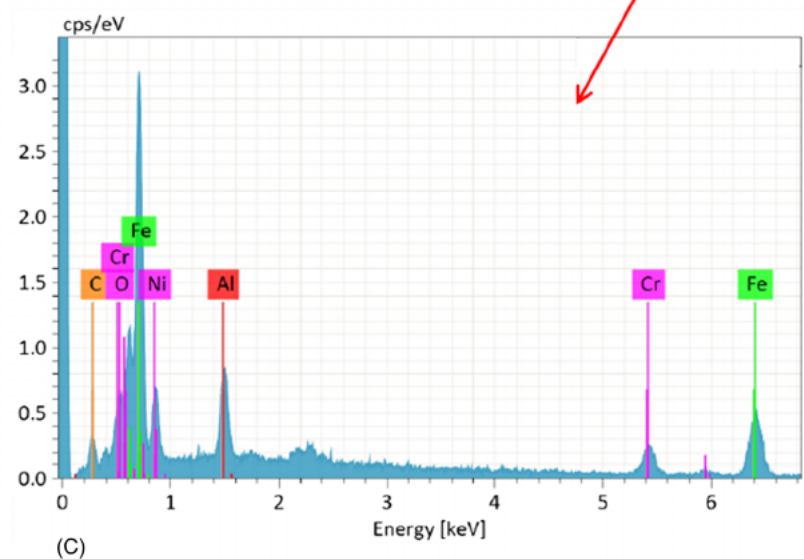
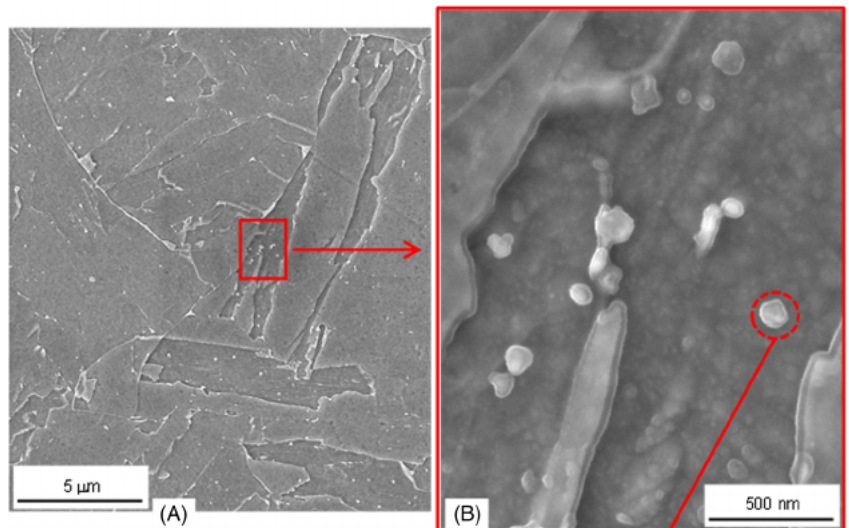
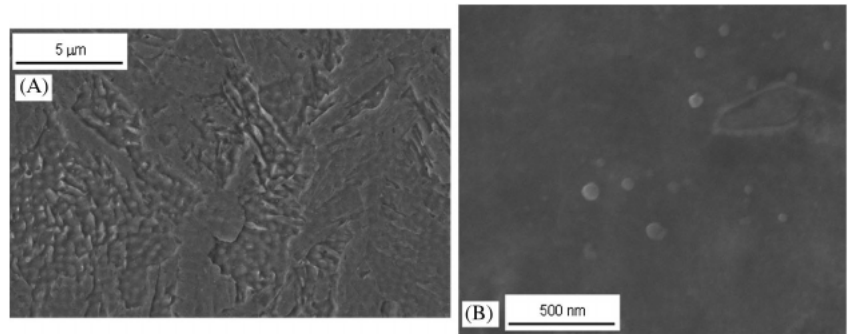


FIGURE 10 Scanning electron microscope (SEM)-FEG observations after heat treatment: (A) elongated grains; (B) detail of (A) with precipitates; (C) precipitate compounds [Colour figure can be viewed at [wileyonlinelibrary.com](https://onlinelibrary.wiley.com)]

a fine equiaxed cellular structure. A similar structure was observed in other samples from not heat treated specimens, regardless of surface orientation with respect to build direction. A detail of precipitates is displayed in Figure 9B. As previously highlighted, the structure of this Maraging Stainless Steel consists of fine nanoprecipitates being uniformly distributed in a martensitic matrix. After the annealing and aging heat treatments, grain boundaries are surrounded by dislocation walls and an important role is given to nanoprecipitates. As an effect of heat

treatments, the existing precipitates (mainly β -NiAl) tend to grow up, while additional ones are induced to nucleate at dislocation tangles. This general growth of precipitates plays an important role for material strengthening.⁴⁶ The observed microstructure in heat treated samples is shown in Figure 10A. It is worth mentioning that heat treatment leads to around 1- μ m-wide elongated grains. As mentioned above, precipitate actual size before and after heat treatment deserves a careful analysis. The annealing and aging treatments lead to precipitate growth from the

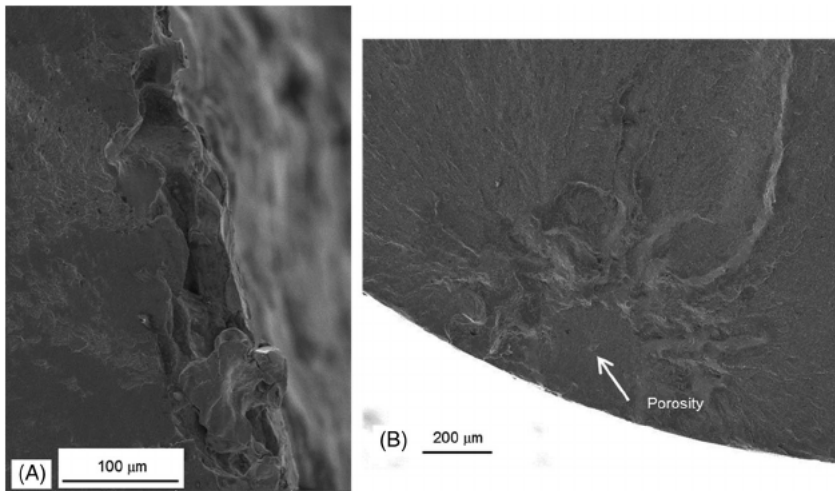


FIGURE 11 Crack initiation points in (A) an unmachined sample. (B) A machined sample with subsurface void

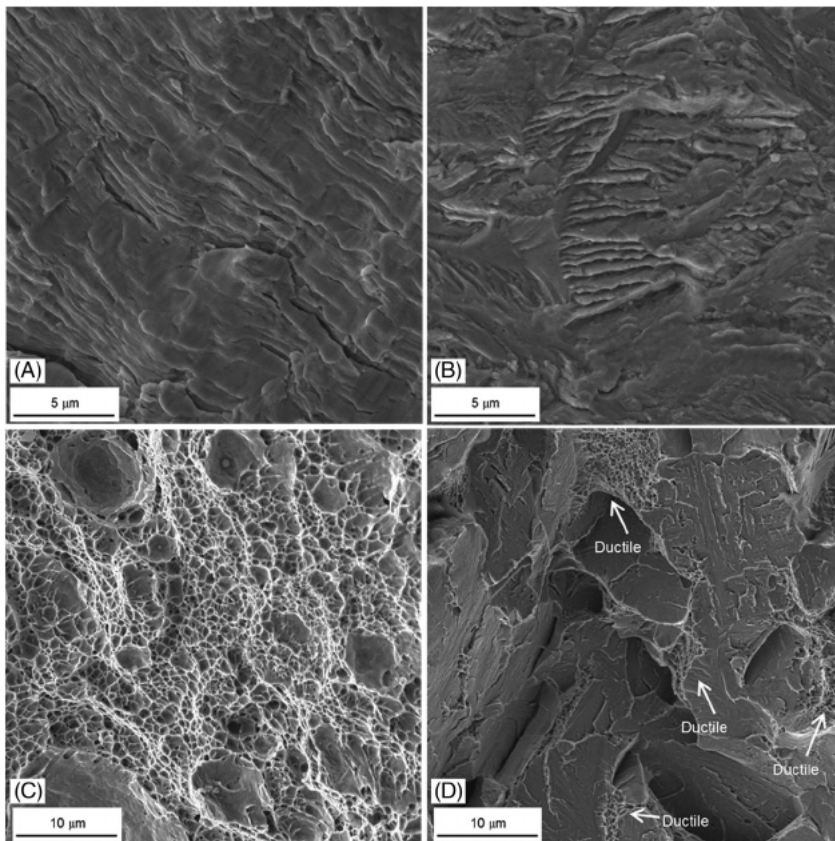


FIGURE 12 (A) Beachmarks in not heat treated conditions. (B) Beachmarks in heat treated conditions. (C) Ductile fracture in not heat treated conditions. (D) Brittle transgranular fracture in heat treated conditions

range 20 to 70 nm to that between 50 and 130 nm. Consistently with the observations in Chang et al.,⁴⁶ this is the most relevant mechanism that leads to strength enhancement against fatigue. A detail of Figure 10A, along with precipitate compounds, is provided in Figure 10B,C.

5.6 | Fracture mechanisms and heat treatment effect investigated by SEM-FEG analyses

The last stage of SEM analysis was devoted to get a full awareness of the fracture mechanism in samples in the unmachined or machined states, with and without heat treatment. Regarding initiation points, it was confirmed that as remarked above^{22,23} high surface roughness in unmachined samples triggers surface crack nucleation, as surface irregularities acted as sharp notches (Figure 11A). Conversely, when considering machined samples, Figure 11B, subsurface voids were usually the primary reason for crack initiation.

Details of beachmarks are respectively provided in Figure 12A,B with regard to not heat treated and treated conditions, respectively. Not significant differences may be observed between the retrieved patterns that also keep the same spacing (300 nm). As for final fracture mode, not heat treated samples exhibited a ductile fracture as clearly highlighted by dimples in Figure 12C with reference to ultimate fracture. Heat treatment had indeed the relevant role of significantly increasing the fatigue strength, but fracture turned to be brittle with transgranular mode (cleavage). This is clearly visible in Figure 12D, although some spots of ductile fracture (highlighted in the same picture) are still present. Material embrittlement is in agreement with hardness increase and toughness drop observed in Chang et al.⁴⁶

6 | CONCLUSIONS

The present study has dealt with the fatigue response of CX Maraging Stainless Steel produced by *PBF*. This is the very first one, going beyond the study of static properties and trying to investigate the response of this material under cyclic loads. The effects of heat treatment and of machining have been experimentally assessed by a two-factor design. Rotating bending tests have led to the determination of *S-N* curves and of fatigue strengths at run-out (corresponding to 10 million lifecycles). The data have been processed by conventional statistical methods, according to Standards, and by a not conventional

ANOVA-based statistical analysis for the comparison of fatigue trends.

The outcomes indicate that both heat treatment and machining have a significantly beneficial effect, even if performed singularly. The effect of the machining is particularly relevant even without heat treatment. It indicates this material is highly sensitive to surface irregularities triggering cracks: running machining leads to a four-time incremented fatigue strength. When heat treatment and machining are applied together (in this order and with subsequent shot-peening), they have a synergic beneficial effect, which leads to a further enhancement of the fatigue strength (up to five times). In this condition, the ratio between the fatigue strength at 10 million cycles and the static resistance (*UTS*) is 0.29, which, also based on previous studies, may be assumed as a reference for Maraging and Stainless Steels. However, when specifically considering the ratio between the fatigue strength at run-out and the actual (in the same condition) ultimate tensile strength, it is worth mentioning that the highest value (0.41) has been obtained, when specimens are machined but not heat treated (with subsequent shot-peening). This seems to be the most effective combination of the investigated parameters for the additively manufactured CX Maraging Stainless Steel also because its fatigue strength keeps very close to the highest one retrieved for the heat treated and machined samples (450 MPa against 510 MPa). In addition, machining has the capability of removing the contour layers and smoothing the external surface, thus moving initiation sites from the surface to inner layers (up to the depth of 0.5 mm).

Electron microscope observations made it possible to assess the heat treatment fatigue strengthening effect. When in its as-built state, the material consists of columnar or equiaxed cells with nanoprecipitates being uniformly spread in the matrix. The precipitation size is incremented upon the two-stage heat treatment; in addition, new precipitates tend to nucleate at dislocation tangles and then to grow up. This mechanism leads to hardness and static and fatigue strength increment. On the other hand, further observations regarding the fracture mode indicate that it is made more brittle, as an effect of heat treatment.

ACKNOWLEDGMENTS

The research presented in the paper represents a part of research carried out within the project “Advanced design rules for optimal dynamic properties of additive manufacturing products – A_MADAM”. This project has received funding from the European Union’s Horizon 2020 research and innovation program under the Marie Skłodowska-Curie grant agreement No 734455: The

authors wish to acknowledge the financial support by the European Commission. The authors from Serbia (S.Ć-K, N.B., and Z.Š) are obliged to acknowledge the support of Ministry of Education, Science and Technology Development of Republic of Serbia to its institution through grant No. 451-03-68/2020-14/200108. Open Access Funding provided by Università di Bologna within the CRUI-CARE Agreement.

AUTHOR CONTRIBUTIONS

Methodology: G.O. and D.C.; sample fabrication and postprocessing: N.B., S.C.K., and Z.S.; fatigue testing: G.O., M.D.A, S.F., F.R., and L.P.; data statistical processing: G.O. and L.P.; data discussion: G.O. and D.C.; microscopy observation: G.O. and L.P.; paper (original version) writing: G.O. and L.P.; paper (revised version) writing: G.O.; supervision: G.O. and D.C.; funding acquisition: S.C.K., Z.S., and D.C.

DATA AVAILABILITY STATEMENT

The data that support the findings of this study are available from the corresponding author upon reasonable request.

NOMENCLATURE

AM	Additive manufacturing
ANOVA	Analysis of variance
b_0, b_1	$S-N$ curve coefficients according to standard
C_b, C_2	Column means (for ANOVA computations)
DMLS	Direct metal laser sintering
FL	Fatigue limit (or strength) at 10 million cycles
HRC	Rockwell hardness
N	Lifecycles (for $S-N$ curve)
PBF	Powder bed fusion
R	Stress ratio (fatigue tests)
$R_i C_j$	Interaction term (for ANOVA computations)
R_a	Roughness average [μm]
R_1, R_2	Row means (for ANOVA computations)
SLM	Selective laser melting
S	Maximum bending stress (for $S-N$ curve)
S_{HM}	10-base logarithm of stress, for Set HM (for ANOVA computations)
S_{HN}	10-base logarithm of stress, for Set HN (for ANOVA computations)
S_{MN}	10-base logarithm of stress, for Set MN (for ANOVA computations)
S_{NN}	10-base logarithm of stress, for Set NN (for ANOVA computations)
\bar{S}	Overall mean (for ANOVA computations)
$S-N$ curve	Maximum bending stress versus life cycles curve in the finite life domain
SSBC	Sum of squares between columns (for ANOVA computations)

SSE	Sum of squares error (for ANOVA computations)
SSI	Sum of squares interaction (for ANOVA computations)
SSBR	Sum of squares between rows (for ANOVA computations)
UTS	Ultimate tensile strength (MPa)
YP	Yield point (MPa)

ORCID

Snežana Ćirić-Koščić  <https://orcid.org/0000-0002-9684-0850>
 Dario Croccolo  <https://orcid.org/0000-0002-5725-5624>
 Massimiliano De Agostinis  <https://orcid.org/0000-0001-5643-1860>
 Stefano Fini  <https://orcid.org/0000-0002-8395-5536>
 Giorgio Olmi  <https://orcid.org/0000-0002-1978-8032>
 Luca Paiardini  <https://orcid.org/0000-0002-0643-6951>
 Francesco Robusto  <https://orcid.org/0000-0003-2456-7880>
 Zlatan Šoškić  <https://orcid.org/0000-0002-2241-4568>
 Nebojša Bogojević  <https://orcid.org/0000-0003-3951-3519>

REFERENCES

- Akyildiz HK, Kulekci MK, Esme U. Influence of shot peening parameters on high-cycle fatigue strength of steel produced by powder metallurgy process. *Fatigue Fract Eng Mater Struct*. 2015;38(10):1246-1254.
- Chen C, Xie Y, Yan X, et al. Effect of hot isostatic pressing (HIP) on microstructure and mechanical properties of Ti6Al4V alloy fabricated by cold spray additive manufacturing. *Addit Manuf*. 2019;27:595-605.
- Nicoletto G. Anisotropic high cycle fatigue behavior of Ti-6Al-4V obtained by powder bed laser fusion. *Int J Fatigue*. 2017;94:255-262.
- Yin S, Chen C, Yan X, et al. The influence of aging temperature and aging time on the mechanical and tribological properties of selective laser melted maraging 18Ni-300 steel. *Addit Manuf*. 2018;22:592-600.
- Becker TH, Dimitrov D. The achievable mechanical properties of SLM produced maraging steel 300 components. *Rapid Prototyp J*. 2016;22(3):487-494.
- Abe F, Osakada K, Shiomi M, Uematsu K, Matsumoto M. The manufacturing of hard tools from metallic powders by selective laser melting. *J Mater Process Technol*. 2001;111(1-3):210-213. [https://doi.org/10.1016/S0924-0136\(01\)00522-2](https://doi.org/10.1016/S0924-0136(01)00522-2)
- Kruth J, Mercelis P, Van Vaerenbergh J, Froyen L, Rombouts M. Binding mechanisms in selective laser sintering and selective laser melting. *Rapid Prototyp J*. 2005;11(1):26-36.
- Nicoletto G. Directional and notch effects on the fatigue behaviour of as-built DMLS Ti6Al4V. *Int J Fatigue*. 2018;106:124-131.
- Kempen K, Thijs L, Van Humbeeck J, Kruth J. Mechanical properties of AlSi10Mg produced by selective laser melting. *Phys Procedia*. 2012;39:439-446.

10. Rosenthal I, Stern A, Frage F. Microstructure and mechanical properties of AlSi10Mg parts produced by the laser beam additive manufacturing (AM) technology. *Metallogr Microstruct Anal.* 2014;3(6):448-453.
11. Maamoun AH, Xue YF, Elbestawi MA, Veldhuis SC. The effect of selective laser melting process parameters on the microstructure and mechanical properties of Al6061 and AlSi10Mg alloys. *Materials.* 2019;12(1):12.
12. Niemann G, Winter H, Hohn BR. *Maschinenelemente.* Germany: Springer-Verlag; 2005.
13. Croccolo D, De Agostinis M, Fini S, Olmi G, Bogojevic N, Ciric-Kostic S. Effects of build orientation and thickness of allowance on the fatigue behaviour of 15–5 PH stainless steel manufactured by DMLS. *Fatigue Fract Eng Mater Struct.* 2018; 41(4):900-916.
14. Croccolo D, De Agostinis M, Fini S, Olmi G, Vranic A, Ciric-Kostic S. Influence of the build orientation on the fatigue strength of EOS maraging steel produced by additive metal machine. *Fatigue Fract Eng Mater Struct.* 2016;39(5):637-647.
15. Li Y, Gu D. Thermal behavior during selective laser melting of commercially pure titanium powder: Numerical simulation and experimental study. *Addit Manuf.* 2014;1:99-109.
16. Brandl E, Heckenberger U, Holzinger V, Buchbinder D. Additive manufactured AlSi10Mg samples using selective laser melting (SLM): Microstructure, high cycle fatigue, and fracture behavior. *Mater Des.* 2012;34:159-169.
17. Leuders S, Thöne M, Riemer A, et al. On the mechanical behaviour of titanium alloy TiAl6V4 manufactured by selective laser melting: Fatigue resistance and crack growth performance. *Int J Fatigue.* 2013;48:300-307.
18. Aboulkhair NT, Maskery I, Tuck C, Ashcroft I, Everitt NM. The microstructure and mechanical properties of selectively laser melted AlSi10Mg: The effect of a conventional T6-like heat treatment. *Mater Sci Eng A.* 2016;667:139-146.
19. Li W, Li S, Liu J, et al. Effect of heat treatment on AlSi10Mg alloy fabricated by selective laser melting: Microstructure evolution, mechanical properties and fracture mechanism. *Mater Sci Eng A.* 2016;663:116-125.
20. Gockel J, Sheridan L, Koerper B, Whip B. The influence of additive manufacturing processing parameters on surface roughness and fatigue life. *Int J Fatigue.* 2019;124:380-388.
21. Braun M, Mayer E, Kryukov I, et al. Fatigue strength of PBF-LB/M and wrought 316L stainless steel: Effect of post-treatment and cyclic mean stress. *Fatigue Fract Eng Mater Struct.* 2021;44(11):1-17. <https://doi.org/10.1111/ffe.13552>
22. Watring DS, Carter KC, Crouse D, Raeymaekers B, Spear AD. Mechanisms driving high-cycle fatigue life of as-built Inconel 718 processed by laser powder bed fusion. *Mater Sci Eng A.* 2019;761:137993.
23. Zhang J, Fatemi A. Surface roughness effect on multiaxial fatigue behavior of additive manufactured metals and its modeling. *Theor Appl Fract.* 2019;103:102260.
24. Vayssette B, Saintier N, Brugger C, El May M, Pessard E. Numerical modelling of surface roughness effect on the fatigue behavior of Ti-6Al-4V obtained by additive manufacturing. *Int J Fatigue.* 2019;123:180-195.
25. Hackel L, Rankin JR, Rubenchik A, King WE, Matthews M. Laser peening: A tool for additive manufacturing post-processing. *Addit Manuf.* 2018;24:67-75.
26. Aguado-Montero S, Navarro C, Vazquez J, Lasagni F, Slawik S, Domínguez J. Fatigue behaviour of PBF additive manufactured Ti6Al4V alloy after shot and laser peening. *Int J Fatigue.* 2022; 154:106536.
27. Kumar P, Ramamurty U. High cycle fatigue in selective laser melted Ti-6Al-4V. *Acta Mater.* 2020;194:305-320.
28. O'Brien JM, Montgomery S, Yaghi A, Afazov SM. Process chain simulation of laser powder bed fusion including heat treatment and surface hardening. *CIRP J Manuf.* 2021;32: 266-276.
29. Kaynak Y, Kitay O. The effect of post-processing operations on surface characteristics of 316L stainless steel produced by selective laser melting. *Addit Manuf.* 2019;26:84-93.
30. Khan HM, Karabulut Y, Kitay O, Kaynak Y, Jawahir IS. Influence of the post-processing operations on surface integrity of metal components produced by laser powder bed fusion additive manufacturing: A review. *Mach Sci Technol.* 2021;25(1): 118-176.
31. Almangour B, Yang J-M. Integration of heat treatment with shot peening of 17-4 stainless steel fabricated by direct metal laser sintering. *JOM.* 2017;69(11):2309-2313.
32. Todai M, Nakano T, Liu T, et al. Effect of building direction on the microstructure and tensile properties of Ti-48Al-2Cr-2Nb alloy additively manufactured by electron beam melting. *Addit Manuf.* 2017;13:61-70.
33. Croccolo D, De Agostinis M, Fini S, et al. Sensitivity of direct metal laser sintering maraging steel fatigue strength to build orientation and allowance for machining. *Fatigue Fract Eng Mater Struct.* 2019;42(1):374-386.
34. Croccolo D, De Agostinis M, Fini S, et al. Fatigue response of as-built DMLS maraging steel and effects of aging, machining, and peening treatments. *Metals.* 2018;8(7):505.
35. Kempen K, Yasa E, Thijs L, Kruth JP, Van Humbeeck J. Microstructure and mechanical properties of selective laser melted 18Ni-300 steel. *Phys Procedia.* 2011;12:255-263.
36. Meneghetti G, Rigon D, Gennari C. An analysis of defects influence on axial fatigue strength of maraging steel specimens produced by additive manufacturing. *Int J Fatigue.* 2019;118: 54-64.
37. Suryawanshi J, Prashanth KG, Ramamurty U. Tensile, fracture, and fatigue crack growth properties of a 3D printed maraging steel through selective laser melting. *J Alloys Compd.* 2017;725: 355-364.
38. Nezhadfar PD, Shamsaei N, Phan N. Enhancing ductility and fatigue strength of additively manufactured metallic materials by preheating the build platform. *Fatigue Fract Eng Mater Struct.* 2021;44(1):257-270. <https://doi.org/10.1111/ffe.13372>
39. Yadollahi A, Mahmoudi M, Elwany A, Doude H, Bian L, Newman JC Jr. Fatigue-life prediction of additively manufactured material: Effects of heat treatment and build orientation. *Fatigue Fract Eng Mater Struct.* 2020;43(4):831-844. <https://doi.org/10.1111/ffe.13200>
40. Erlach SD, Leitner H, Bischof M, et al. Comparison of NiAl precipitation in a medium carbon secondary hardening steel and C-free PH13-8 maraging steel. *Mater Sci Eng A.* 2006; 429(1-2):96-106.
41. EOS GmbH – Electro Optical Systems. *Material Data Sheet: EOS Stainless Steel CX.* Germany: <http://www.eos.info>, 2017.

42. Asgari H, Mohammadi M. Microstructure and mechanical properties of stainless steel CX manufactured by Direct Metal Laser Sintering. *Mater Sci Eng A*. 2018;709:82-89.
43. Guo Z, Sha W, Vaumousse D. Microstructural evolution in a PH13-8 stainless steel after ageing. *Acta Mater*. 2003;51(1):101-116.
44. Sanjari M, Hadadzadeh A, Pirgazi H, et al. Selective laser melted stainless steel CX: Role of built orientation on microstructure and micro-mechanical properties. *Mater Sci Eng A*. 2020;786:139365.
45. Hadadzadeh A, Shahriari A, Amirkhiz BS, Li J, Mohammadi M. Additive manufacturing of an Fe–Cr–Ni–Al maraging stainless steel: Microstructure evolution, heat treatment, and strengthening mechanisms. *Mater Sci Eng A*. 2020;787:139470.
46. Chang C, Yan X, Bolot R, et al. Influence of post-heat treatments on the mechanical properties of CX stainless steel fabricated by selective laser melting. *J Mater Sci*. 2020;55(19):8303-8316.
47. Shahriari A, Khaksar L, Nasiri A, Hadadzadeh A, Amirkhiz BS, Mohammadi M. Microstructure and corrosion behavior of a novel additively manufactured maraging stainless steel. *Electrochim Acta*. 2020;339:135925.
48. Harvey RF, Lake O. Precipitation hardening steel, 1972.
49. Utsunomiya T, Hoshino K, Hirotsu S. Martensitic precipitation-hardenable stainless steel, 1991.
50. Sanz C, Garcia Navas V, Gonzalo O, Vansteenkiste G. Study of surface integrity of rapid manufacturing parts after different thermal and finishing treatments. *1st CIRP Conference on Surface Integrity Proceedings*. 2011;19:294–299.
51. Zaeh M, Ott M. Investigation on heat regulation of additive manufacturing processes for metal structures. *CIRP Ann Manuf Technol*. 2011;60(1):259-262.
52. Santos E, Masanari S, Osakada K, Laoui T. Rapid manufacturing of metal components by laser forming. *Int J Mach Tool Manuf*. 2006;46(12-13):1459-1468.
53. Safai L, Sebastian Cuellar J, Smit G, Zadpoor AA. A review of the fatigue behavior of 3D printed polymers. *Addit Manuf*. 2019;28:87-97.
54. ASTM E466-15. *Standard Practice for Conducting Force Controlled Constant Amplitude Axial Fatigue Tests of Metallic Materials*. West Conshohocken, PA, United States: ASTM International; 2015.
55. Dixon WJ, Massey F Jr. *Introduction to Statistical Analysis*. United States: McGraw-Hill; 1983.
56. Van Hooreweder B, Moens D, Boonen R, Sas P. The critical distance theory for fatigue analysis of notched aluminium specimens subjected to repeated bending. *Fatigue Fract Eng Mater Struct*. 2012;35(9):878-884.
57. ASTM E18-16. *Standard Test Methods for Rockwell Hardness of Metallic Materials*. West Conshohocken, PA, United States: ASTM International; 2016.
58. Branco R, Costa JDM, Berto F, et al. Low-cycle fatigue behaviour of AISI 18Ni300 maraging steel produced by selective laser melting. *Metals*. 2018;8(1):32.
59. Olmi G. Low cycle fatigue experiments on Turbogenerator steels and a new method for defining confidence bands. *J Test Eval*. 2012;40(4). Paper ID JTE104548.
60. Maskery I, Aboulkhair NT, Corfield MR, et al. Quantification and characterisation of porosity in selectively laser melted al-Si10-mg using X-ray computed tomography. *Mater Charact*. 2016;111:193-204.

How to cite this article: Ćirić-Koščić S, Croccolo D, De Agostinis M, et al. Fatigue response of additively manufactured Maraging Stainless Steel CX and effects of heat treatment and surface finishing. *Fatigue Fract Eng Mater Struct*. 2021; 1-18. doi:10.1111/ffe.13611